Check for updates

ADVANCED FUNCTIONAL MATERIALS
www.afm-journal.de

Precision Interface Engineering of CuNi Alloys by Powder ALD Toward Better Thermoelectric Performance

Shiyang He, Amin Bahrami, Chanwon Jung, Xiang Zhang, Ran He, Zhifeng Ren, Siyuan Zhang, and Kornelius Nielsch**

The main bottleneck in obtaining high-performance thermoelectric (TE) materials is identified as how to decouple the strong interrelationship between electrical and thermal parameters. Herein, a precise interface modification approach based on the powder atomic layer deposition (ALD) technology is presented to enhance the performance of CuNi alloys. ZnO and Al_2O_3 layers as well as their combinations are deposited on the surface of powders, typically in 10–100 ALD cycles, and their effects on the TE performance of bulks is thoroughly investigated. The enhancement of the Seebeck coefficient, caused by the energy filtering effect, compensates for the electrical conductivity deterioration due to the low electrical conductivity of oxide layers. Furthermore, the oxide layers may significantly increase the phonon scattering. Therefore, to reduce the resistivity of coating layer, a multilayer structure is deposited on the surface of powders by inserting Al_2O_3 into ZnO. The accurate microstructure characterization shows that the Al atoms diffused into ZnO and realized the doping effect after pressing. Al diffusion has the potential to increase the electrical conductivity and complexity of coating layers. Compared to pure CuNi, *zT* increases by 128% due to the decrease in resistivity and stronger phonon scattering in phase boundaries.

1. Introduction

Thermoelectric (TE) materials, as a direct energy conversion between heat and electricity, are one of the promising solutions for the impending energy problem and environmental degradation.[1,2] The conversion efficiency of TE devices is mainly dominated by the dimensionless figure of merit zT,[3–5] which can be expressed as $zT = S^2T/[\rho(\kappa_{ele}+\kappa_{lat})]$, where S, ρ, κ_{ele}, κ_{lat}, T are the Seebeck coefficient, resistivity, electrical thermal conductivity, lattice thermal conductivity, and absolute temperature, respectively. Thus, the performance of TE materials is jointly determined by their electrical and thermal transport properties.

Manipulating the grain boundaries to chase favorable transport properties is an essential issue in designing thermoelectric materials.[6,7] The chemical compositions and physical properties of the grain boundaries have a substantial effect on the TE performance.[8,9] Thus, the introduction of new phases into the matrix on the grain boundaries to form multiphase composites is another prominent approach attracting major scientific interests.[10–12] In thermoelectric materials, two approaches are introduced to construct multiphase composites[13]: i) forming precipitations in non-equilibrium conditions during the melting and solidification of the parent compound[14,15] and ii) artificial second phase additions by dispersing the nanoparticles or forming a core-shell structure.[16,17] The approaches mentioned above enable the combination of different dispersions and matrices in such a way that two or more constituents can be gathered in one system, endowing the final system with its own advantageous characteristics.[18–21] However, to achieve better TE performance, the composition and

S. He, A. Bahrami, R. He, K. Nielsch
Institute for Metallic Materials
Leibniz Institute for Solid State and Materials Research
01069 Dresden, Germany
E-mail: a.bahrami@ifw-dresden.de; k.nielsch@ifw-dresden.de

S. He, K. Nielsch
Institute of Materials Science
Technische Universität Dresden
01062 Dresden, Germany

The ORCID identification number(s) for the author(s) of this article can be found under https://doi.org/10.1002/adfm.202314457

© 2024 The Authors. Advanced Functional Materials published by Wiley-VCH GmbH. This is an open access article under the terms of the Creative Commons Attribution License, which permits use, distribution and reproduction in any medium, provided the original work is properly cited.

DOI: 10.1002/adfm.202314457

C. Jung, S. Zhang
Max-Planck-Institut für Eisenforschung GmbH
40237 Düsseldorf, Germany

X. Zhang
National Center for International Joint Research of Micro-Nano Molding Technology
School of Mechanics and Safety Engineering
Zhengzhou University
Zhengzhou 450001, China

Z. Ren
Department of Physics and Texas Center for Superconductivity at the University of Houston (TcSUH)
University of Houston
Houston 77204, USA

content of the second phase must be precisely controlled, even at the atomic scale, which is challenging to achieve using existing approaches.[13] Atomic layer deposition (ALD) is recognized as a unique layer-by-layer deposition technique for creating highly homogenous films in a controlled manner.[22,23] Unlike chemical vapor deposition, the precursors in ALD are always separated and alternatively pulsed into reactors to achieve layer-by-layer growth.[24,25] Because of the self-limiting nature of the chemical reactions in an ALD process, not only film thickness can be controlled down to the atomic level, allowing for the deposition of extremely thin films (even only a few atoms thick),[17,26] but also a highly conformal coating can be expected.[16,27] Furthermore, the separated pulsing process allows for the formation of multilayer structures, which can be used to accurately tune the compositions of films.[28] These characteristics enable ALD to precisely deposit a specific thickness of selected materials on the surface of thermoelectric powders in order to manipulate the transport properties of the selected material. pALD has already demonstrated unprecedented success in improving the TE performance of various TE materials, such as Bi,[29,30] Bi_2Te_3 alloys,[31,32] $CoSb_3$,[33] and ZrNiSn-based materials.[34] Different oxides, such as Al_2O_3,[30] TiO_2,[35] and ZnO[33] are mainly used as coating layers due to their developed deposition process and good thermal stability.

However, it might be difficult to achieve high zT when utilizing a single compound oxide layer as the particle surface modifier. In terms of transport properties of the modified compound, the ρ, κ, and thickness of coating layers (x) define the electrical and thermal conduction between the oxide and main phase boundaries. For instance, for a given coating layer with low ρ, less degradation effect on the overall electrical conductivity is expected. However, the thicker layers of the coating compound can cause effective carriers scattering which results in an increment of S and reduction of κ_{tot}, even though considerable electrical conductivity reduction is inevitable. In addition, the oxide layers may form the thermal conduction path if the thickness of the layers is too high. As a result, a compromise between the ρ, κ of coating materials and their thickness (x) should be sought.

Aside from the intrinsic characteristics of the coating compound and its thickness, the architecture and complexity of the coating layer is a criterion that has received little attention. As reported before, inserting TiO_2,[36] HfO_2,[36] or Al_2O_3[37] into ZnO layers with multilayer structures after annealing can significantly reduce the ρ of the film compared to pristine ZnO. Having a multilayer coating in the particle junction might be beneficial considering two aspects: i) by decreasing the ρ of coating and allowing to deposit of a higher thickness of coating layer to enhance S and ii) complex interfaces might induce stronger phonon scattering compared to a single layer oxide coating.

Herein, we employ ALD-based interface modification to optimize the thermal and electrical transport properties of the CuNi thermoelectric material trying to decouple the thermoelectric parameters. The reason we choose CuNi is because of its very high power factor (>50 mW m^{-1} K^{-2}) and its very high thermal conductivity (>37 W m^{-1} K^{-1}) in high-temperature range. The effect of a single layer of ZnO and Al_2O_3 oxides and multilayers of $ZnO/Al_2O_3/ZnO$ on TE properties has been thoroughly investigated as listed in **Table 1**. The presence of ZnO and Al_2O_3layers on CuNi, contributes to the creation of an energy barrier by the oxide layer, resulting in a significant rise in the S. Although there is an insignificant decrease in ρ, the enhanced S after 50 cycles ALD of ZnO compensated for the loss and resulted in ≈45% increment of PF compared to the pristine sample. In addition, the multilayer structure of $ZnO/Al_2O_3/ZnO$ was constructed on the surface of the powder to enhance electrical resistance at phase boundaries (**Figure 1**). In high cycle number coating (>50 cycles), the multilayer coatings maintained the high PF while significantly reducing the thermal conductivity. For the sample modified with Z44/A11/Z44 multilayers, due to decoupling thermoelectric parameters by ALD, a maximum figure of merit (zT) of 0.22 was achieved at 673 K, ≈128% higher than that of pristine CuNi and is a bit higher than the previously reported vaules[38–44] (**Figure 2**).

Table 1. The summaries of ALD coating layers are in this work.

Types of ALD layers	Compositions of ALD layers	Cycle numbers of coating layers	Nomenclature
Single layer	Al_2O_3	10	A10
		20	A20
		50	A50
		100	A100
	ZnO	10	Z10
		20	Z20
		50	Z50
		100	Z100
Multilayers	$ZnO/Al_2O_3/ZnO$	20/5/20	Z20/A5/Z20
		28/7/28	Z28/A7/Z28
		44/11/44	Z44/A11/Z44

2. Results and Discussion

2.1. Analysis of the CuNi Powder Coated with ZnO and Al_2O_3

To systematically investigate the effects of ALD coating layers on TE performance, the microstructure and the composition of ALD thin films and coated powders should be first explored.

Analyses of X-ray reflectometry (XRR) measurement data to a simulated curve indicate a density of 5.6 and 3.0 g cm^{-3} and a thickness of 61.1 and 43.2 nm for 300 cycles ALD of ZnO and Al_2O_3 thin films on Si substrate, respectively, as shown in Figure S1a,b (Supporting Information). The linear increase in thin film thickness on the Si wafer by increasing the number of ALD cycles is shown in Figure S1c (Supporting Information), suggesting a growth per cycle (GPC) of 1.4 and 2.1 Å per cycle for ZnO and Al_2O_3, respectively. This reveals excellent thickness controllability at the sub-nano scale. Additionally, as shown in Figure S1d (Supporting Information), the electrical conductivities of ZnO and Al_2O_3 films in the range of 275–400 K were examined and ZnO films exhibit much higher electrical conductivity which is around five orders of magnitude higher than that of Al_2O_3. The difference in the electrical conductivity of ZnO and Al_2O_3 ALD films may play a vital role in the electrical conduction of the particle boundaries, which have a great influence on the overall resistivity of coated bulk samples.

© 2024 The Authors. Advanced Functional Materials published by Wiley-VCH GmbH

16163028, 2024, 30, Downloaded from https://onlinelibrary.wiley.com/doi/10.1002/adfm.202314457, Wiley Online Library on [26/09/2024]. See the Terms and Conditions (https://onlinelibrary.wiley.com/terms-and-conditions) on Wiley Online Library for rules of use; OA articles are governed by the applicable Creative Commons License

16163028, 2024, 30, Downloaded from https://onlinelibrary.wiley.com/doi/10.1002/adfm.202314457, Wiley Online Library on [26/09/2024]. See the Terms and Conditions (https://onlinelibrary.wiley.com/terms-and-conditions) on Wiley Online Library for rules of use; OA articles are governed by the applicable Creative Commons License

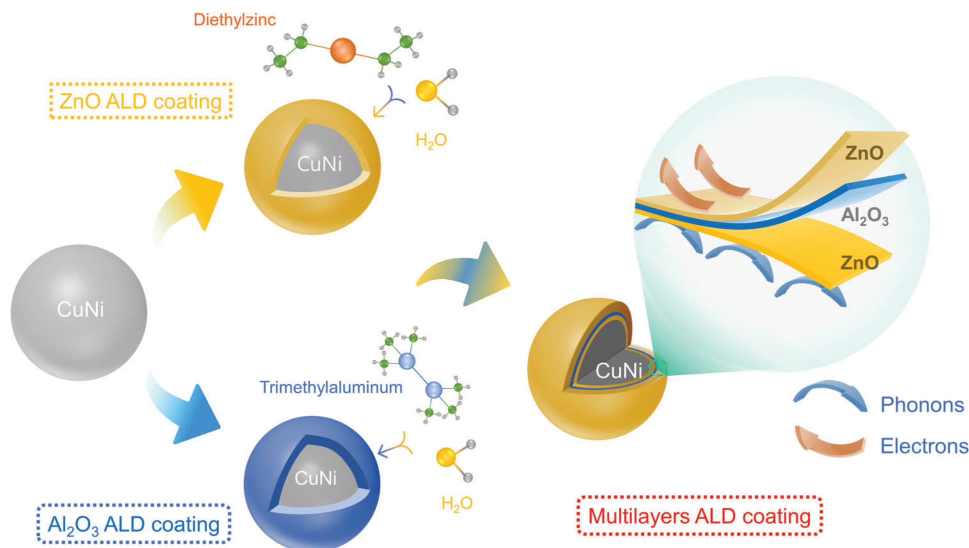

Figure 1. A schematic of ZnO, Al_2O_3, and multilayer structure ($ZnO/Al_2O_3/ZnO$) deposition processes based on powder ALD.

The relationship between the Zn and Al content (wt%) and ALD cycle numbers can be elicited from the mentioned physical parameters of films. The detailed mathematical derivation can be found in Supporting Information Note. It should be noted that the wt% is proportional to C^3_{layers} and R^{-1}_{CuNi}, where C_{layer} is the ALD cycle number and R_{CuNi} is the radius of CuNi particles (Figure S2a, Supporting Information). In this work, the average radius of CuNi particles is considered as 6.5 µm, according to the materials data sheet (Figure S2b, Supporting Information). Considering that all the CuNi particles are

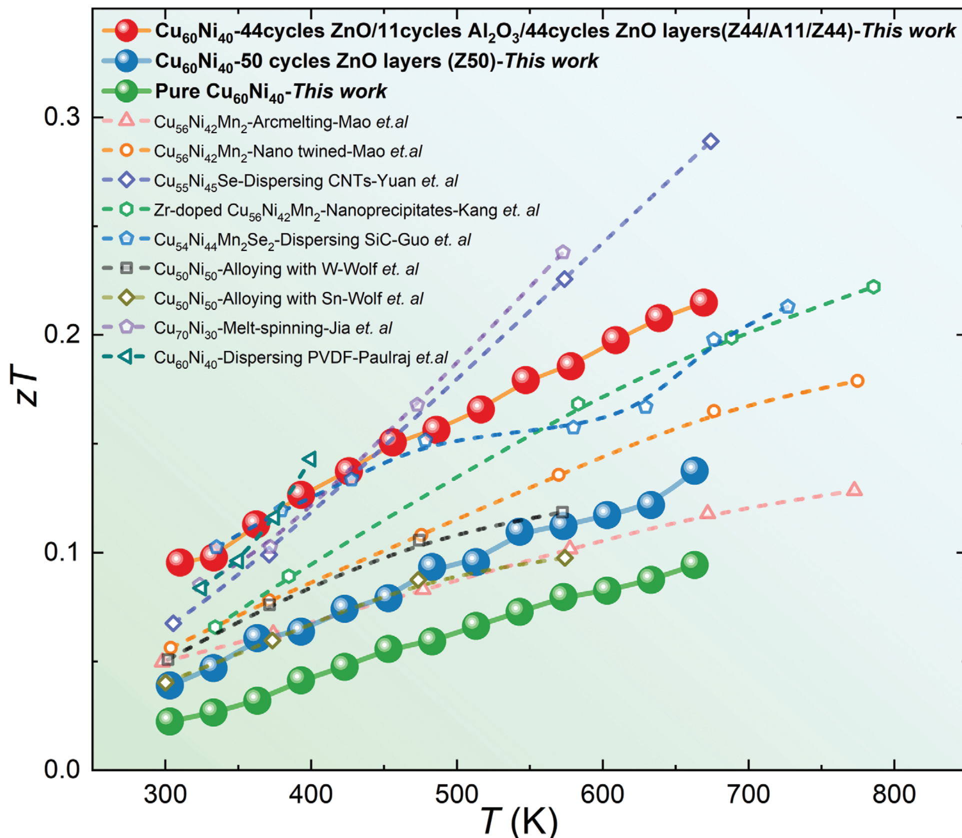

Figure 2. Comparison of temperature-dependent zT among other optimized CuNi works.[38–44]

© 2024 The Authors. Advanced Functional Materials published by Wiley-VCH GmbH

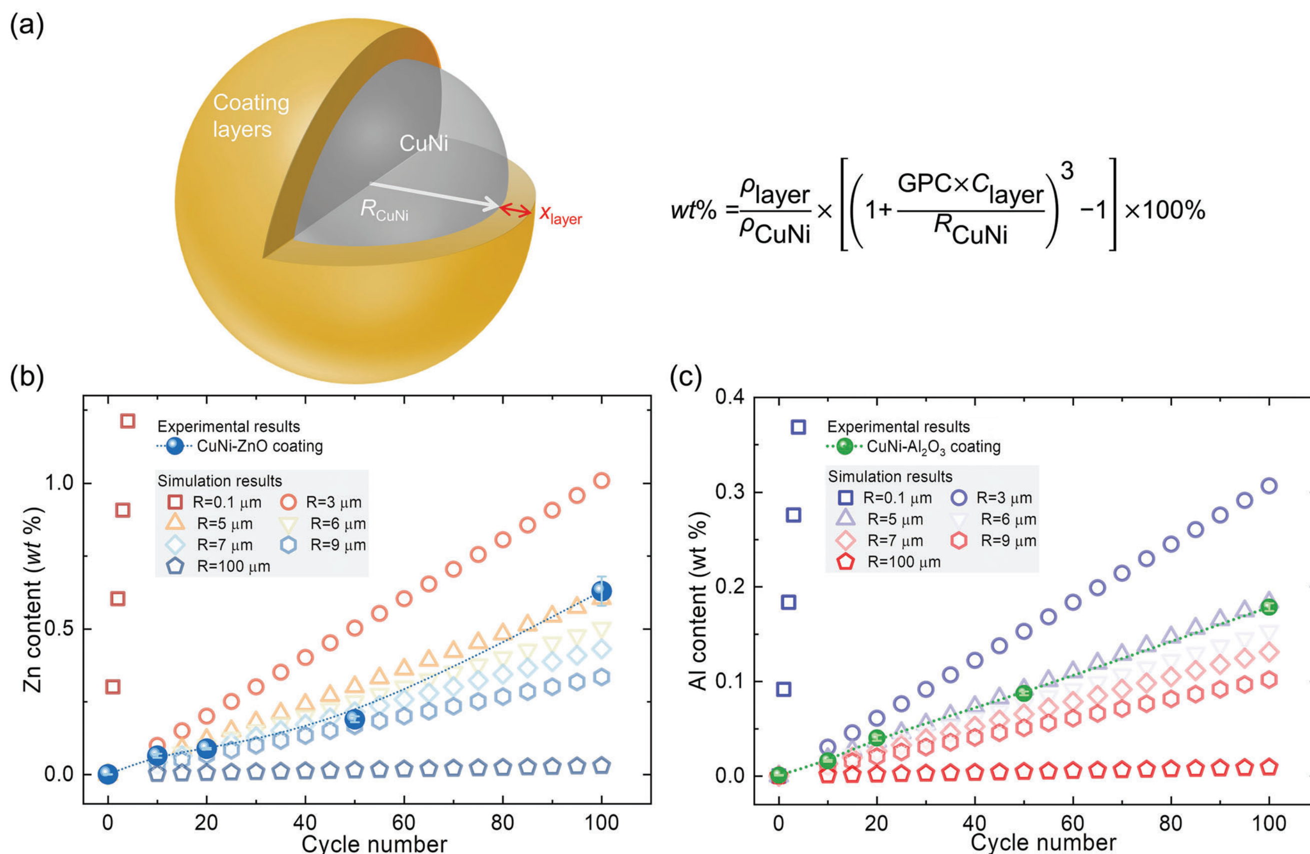

Figure 3. a) The schematic image of coated particles and the calculated relationship between wt% and growth rate per cycle (GPC)/cycle number (C_{layer})/R_{CuNi} (particle radius). b) The cycle number dependence of the weight percentage of Zn. c) The cycle number dependence on the weight percentage of Al.

uniformly coated with ZnO and Al_2O_3 films, the calculated Zn and Al content as a function of the ALD cycle number is presented in **Figure 3**. The Zn and Al contents in the samples coated with different ALD cycle numbers were also measured by inductively coupled plasma-optical emission spectrometry (ICP-OES) and are presented in Figure 3 and Table S1 (Supporting Information). With increasing the ALD cycle number, Zn and Al content increased monotonously. The experimental data fit well with the simulation indicating that the coating layers of ZnO and Al_2O_3 were homogeneously deposited on each particle.

Furthermore, the energy dispersive spectroscopy (EDX) elemental mapping and point analyses performed on the surface of ZnO-coated samples show that the Zn signal from ZnO is uniformly distributed on the surface of every single CuNi particle, as shown in **Figures 4** and S3 (Supporting Information).

2.2. The Effect of Single-Kind Oxides Coated CuNi Bulks on TE Performance

The X-ray diffraction (XRD) patterns of as-sintered samples have been presented in Figure S4 (Supporting Information). All the main diffraction peaks in XRD patterns can be well indexed to $Cu_{0.6}Ni_{0.4}$ with an FCC (space group $Fm\bar{3}m$) structure, consisting of the ICP-OES results. In the XRD patterns of pALD-modified and sintered samples, the ZnO peaks cannot be detected if <50 ALD cycles are used, while it appears clearly in the Z100 sample. It indicates that the crystalline ZnO thin films were successfully deposited on the surface of powders and were not decomposed or formed alloys with CuNi. Due to the amorphous nature or low contents of ALD-Al_2O_3,[30] no diffraction peaks corresponding to Al_2O_3 were detected in the XRD patterns of ALD-Al_2O_3 modified samples.

The effect of single ALD layers of ZnO and Al_2O_3 on the TE performance of CuNi was thoroughly investigated (Figures S5 and S6, Supporting Information). Additionally, the ALD cycle number dependence of TE parameters is summarized in **Figure 5**. As shown in Figure 5a, ρ exhibits a monotonously increasing trend by increasing the cycle numbers at both 300 and 673 K measurement temperatures, indicating effective scattering of charge carriers at the energy barrier induced by the oxides. The ρ of modified CuNi varied from 0.5 to 0.67 µm·Ω when ZnO was deposited, while that in Al_2O_3 coated CuNi rapidly increased and reached 2.07 µm·Ω as the number of ALD cycles increased. This indicates that the chemical composition, crystal structure, and thickness of oxides have different influences on ρ. Also, analysis of additional interfacial electrical resistance induced by the oxide layer at the phase boundary (see Figure S7, Supporting Information) reveals an increase in electrical

© 2024 The Authors. Advanced Functional Materials published by Wiley-VCH GmbH

16163028, 2024, 30, Downloaded from https://onlinelibrary.wiley.com/doi/10.1002/adfm.202314457, Wiley Online Library on [26/09/2024]. See the Terms and Conditions (https://onlinelibrary.wiley.com/terms-and-conditions) on Wiley Online Library for rules of use; OA articles are governed by the applicable Creative Commons License

16163028, 2024, 30, Downloaded from https://onlinelibrary.wiley.com/doi/10.1002/adfm.202314457, Wiley Online Library on [26/09/2024]. See the Terms and Conditions (https://onlinelibrary.wiley.com/terms-and-conditions) on Wiley Online Library for rules of use; OA articles are governed by the applicable Creative Commons License

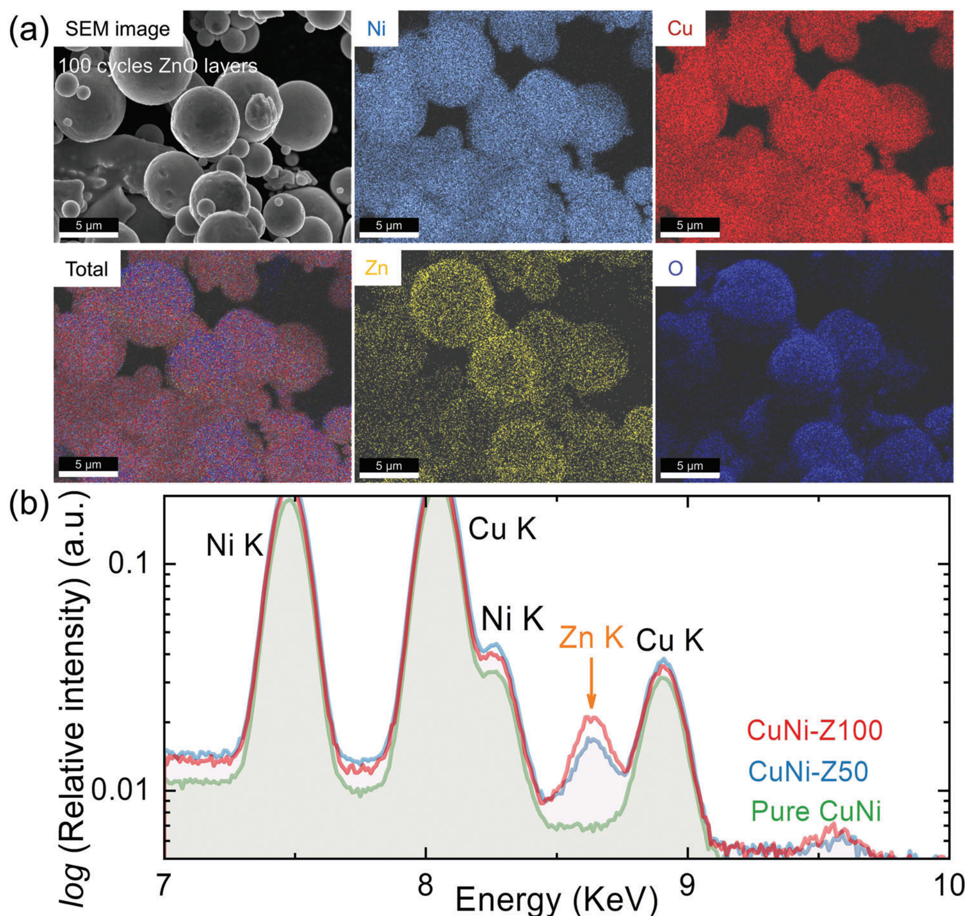

Figure 4. a) EDX element mapping for the Z100 sample. b) The EDX spectrums of pure, Z50, and Z100 samples.

resistance with an escalating cycle number, with the Al_2O_3-coated samples displaying notably higher values. This suggests that the Al_2O_3 coating exerts a more pronounced negative effect on the overall sample electrical conductivities. Figure 5b shows that S is significantly augmented by increasing the cycle numbers from −32 to −45 μV K^{-1} at 300 K and from −55 to −65 μV K^{-1} at 673 K by increasing the cycle numbers. However, a further increase in the ALD cycle numbers (>50 cycles) of both oxides did not cause a further increase of S, similar to S variation in our previous report where Bismuth particles were coated with different oxides.[30] In Z50 samples, the increment of S compensates for the degradation of ρ, resulting in an increment of PF from 1.99 to 3.15 mW $m^{-1}\cdot K^2$ at 300 K. However, due to stronger scattering in Al_2O_3-coated samples, the enhancement of PF only occurred in low cycle number coated samples (<10 cycles) as higher cycle numbers deteriorate PF in Al_2O_3-coated samples (Figure 5c).

The cycle number dependence of κ_{tot} is shown in Figure 5d and shows a monotonous decreasing trend at both 300 and 673 K. The κ_{tot} in the A100 sample achieves a 31.6% decrement while that reduces only 10.5% in the Z100 sample, both measured at 673 K. Because κ_{tot} is the sum of the electronic (κ_{ele}) and lattice (κ_{lat}) constituents ($\kappa_{tot} = \kappa_{lat} + \kappa_{ele}$), the influence of oxide coating layers on the phonon scattering should be evaluated in details. The Wiedemann-Franz law can be used to calculate $\kappa_{ele} = L\sigma T$, where L is the Lorenz number and is described as $L = 1.5 + exp(-|S|/116)$. As shown in Figure 5e, the κ_{lat} of the ZnO-coated sample generally decreased with increasing cycle number. However, in Al_2O_3 modified samples, effective suppression of the κ_{lat} was observed in the A10 sample, reducing the κ_{lat} from 12.5 to 8.7 W $m^{-1}\cdot K$ at 673 K. Beyond 10 ALD cycle of Al_2O_3, the κ_{lat} significantly increased to 19.8 W $m^{-1}\cdot K$ at 673 K A100 sample which is even higher than pristine CuNi. The enormous enhancement of κ_{lat} might be a result of some characteristic changes in Al_2O_3 layers during the sintering process. According to the previous studies,[45–47] the amorphous Al_2O_3 films deposited by ALD at 423 K (150 °C) can be crystallized at temperatures above ≈1098 K (825 °C). It should be noted that Al_2O_3-coated CuNi in this study were pressed at 1073 K (800 °C) and the Al_2O_3 films might be fully or partially crystallized. The ultra-thin Al_2O_3 and ZnO layers deposited by a low number of ALD cycles can be embedded in CuNi as nano-inclusions, enhancing significantly the phonon scattering. However, thicker, more coalescent, and crystalline Al_2O_3 film deposited by the higher number of ALD cycles, as a well-known high κ material, may form the thermal conduction path, leading to a huge increment of κ_{lat}. Due to the enhancement of PF and suppression of κ_{lat}, the zT values augmented from 0.09 to 0.14 and 0.12 at 673 K in Z50 and A10 samples, respectively (Figure 5f).

© 2024 The Authors. Advanced Functional Materials published by Wiley-VCH GmbH

16163028, 2024, 30, Downloaded from https://onlinelibrary.wiley.com/doi/10.1002/adfm.202314457, Wiley Online Library on [26/09/2024]. See the Terms and Conditions (https://onlinelibrary.wiley.com/terms-and-conditions) on Wiley Online Library for rules of use; OA articles are governed by the applicable Creative Commons License

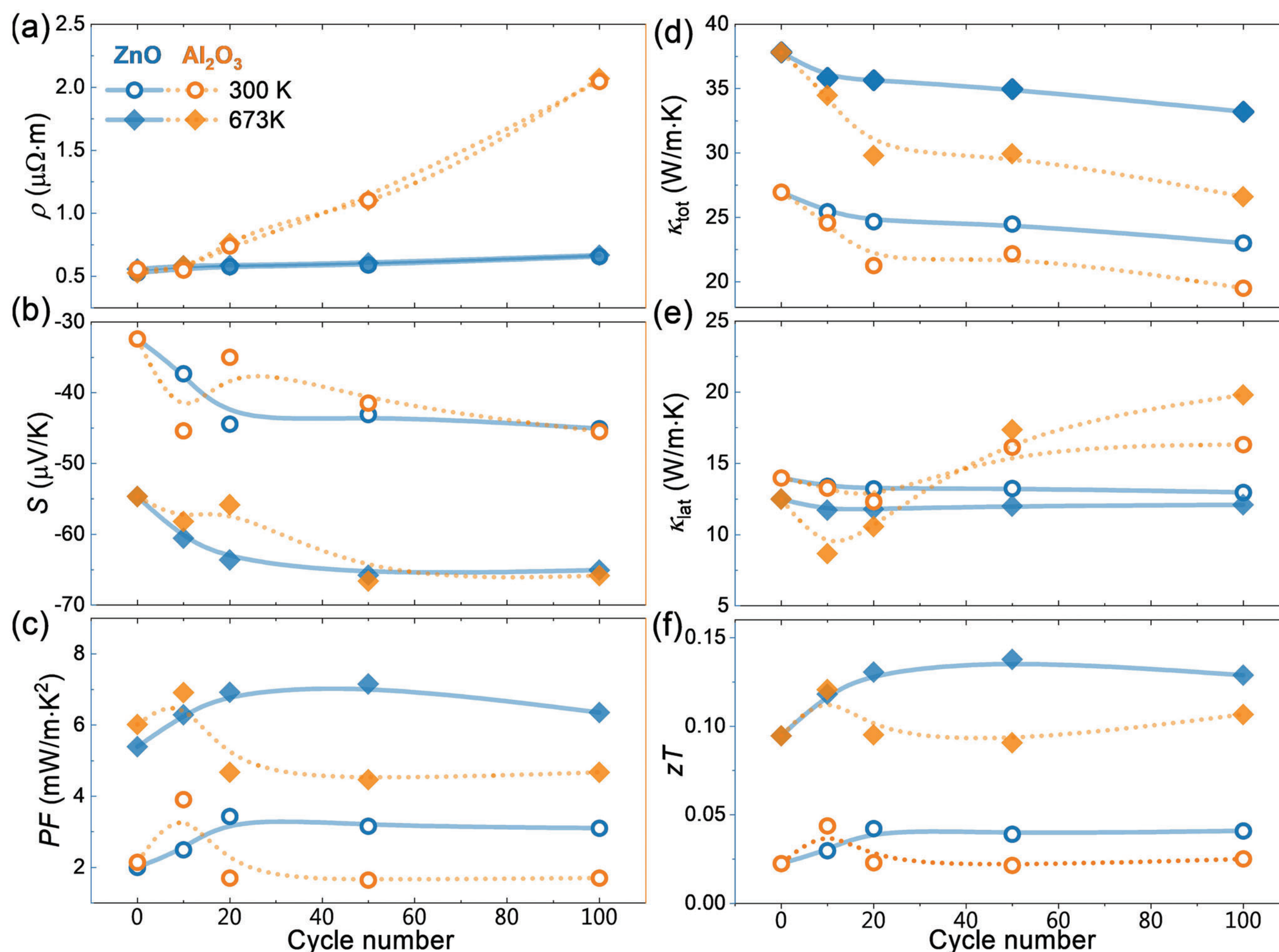

Figure 5. The ZnO and Al_2O_3 cycle number dependence of a) ρ, b) S, c) PF, d) κ_{tot}, e) κ_{lat}, and f) zT at 300 and 673 K.

2.3. Effect of Multilayer Coatings on TE Performance of Bulk CuNi

Considering the results discussed for the CuNi modified with a single oxide layer, it can be concluded that although ρ is increasing constantly by increasing the ZnO and Al_2O_3 ALD cycle numbers and a few ALD cycles (<50 cycles) can trigger significant augmentation of *S*. Also, from the variation of *PF* with the cycle number, it can be concluded that ZnO performs better than Al_2O_3 to optimize electrical properties due to less degradation of electrical conduction. However, the reduction of κ_{lat} in all ZnO-coated samples is not as effective as that of the A10 sample, indicating the strong phonon scattering by Al_2O_3 (amorphous) compared to ZnO (crystalline). It also should be noted that, due to the amorphous-to-crystalline transition, the thicker Al_2O_3 layer (in a higher cycle number of Al_2O_3 layers) might form the thermal conduction path which is not favorable to κ_{lat} suppression.

Therefore, combining ZnO and Al_2O_3 as a multilayer structure might result in the decoupling of TE parameters. To prove that, an ultra-thin Al_2O_3 layer was inserted into ZnO layers to construct the multilayer structure. It can be postulated that using this approach, due to the doping effect, the ρ of multilayer decreased compared to that of pristine ZnO,[37] thus slighter *PF* loss can be expected. Additionally, lower ρ allows for increasing the thickness of layers which is beneficial for suppression of κ_{lat}. Note that, the crystal complexity of multilayers due to the doping effect might cause stronger phonon scattering in the phase boundaries.

The present study has opted for a ZnO: Al_2O_3 ratio of 8:1 to enhance electrical conductivity, as reported in the reference.[37] The effect of multilayer structures with different thicknesses on the TE performance is presented in **Figure 6**. As shown Figure 6a, the ρ increased constantly with increasing the ALD cycle numbers of multilayer constituents. Compared to the Z100 sample, the ρ of the Z44/A11/Z44 sample decreased by 5% in the whole measured temperature range. Also, the lower ρ of the Z20/A5/Z20 sample compared to that of the Z50 sample was observed, which indicates the enhancement of electrical conductivity at phase boundaries after inserting Al_2O_3 layers. Figure 6b indicates that the thickest multilayer possesses a slightly higher absolute *S* compared to thin multilayer and single component layers. The more conductive phase boundaries result in an 11.7% enhancement in *PF* in the Z44/A11/Z44 sample at 673 K when compared to the Z100 sample (Figure 6c). As shown in Figure 6d,e

© 2024 The Authors. Advanced Functional Materials published by Wiley-VCH GmbH

16163028, 2024, 30, Downloaded from https://onlinelibrary.wiley.com/doi/10.1002/adfm.202314457, Wiley Online Library on [26/09/2024]. See the Terms and Conditions (https://onlinelibrary.wiley.com/terms-and-conditions) on Wiley Online Library for rules of use; OA articles are governed by the applicable Creative Commons License

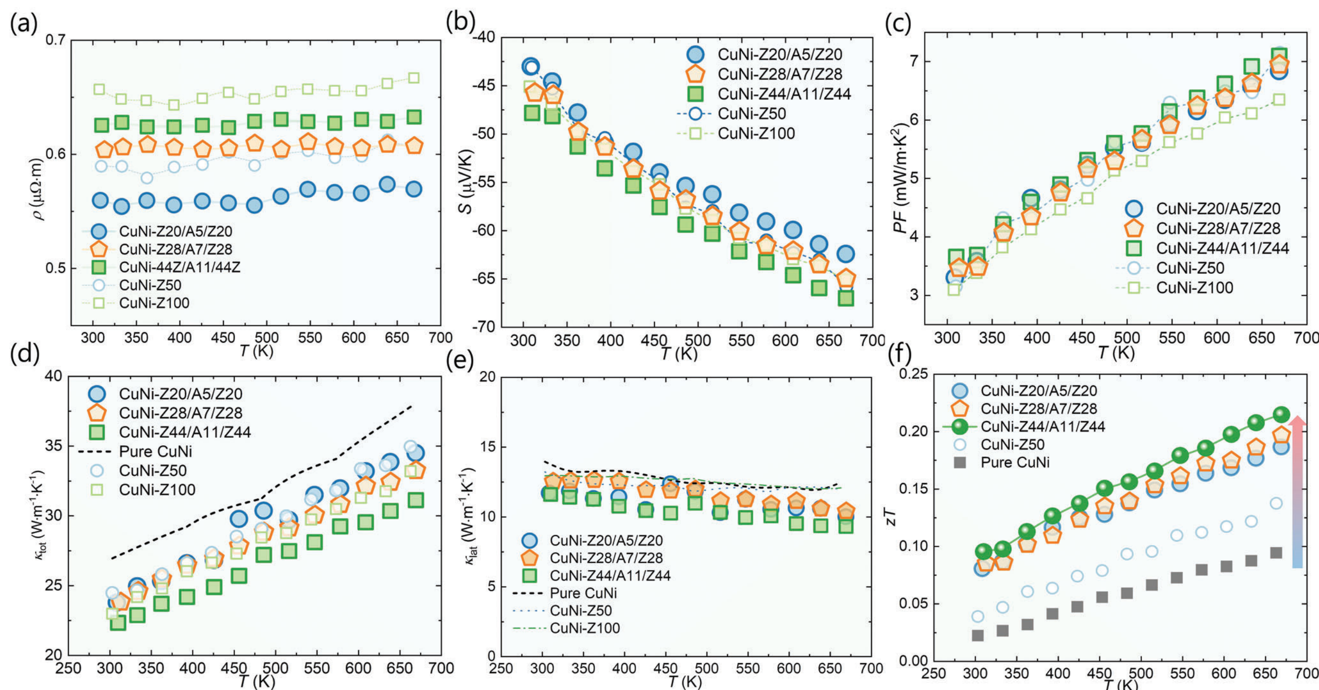

Figure 6. The temperature dependence of a) ρ, b) S, c) PF, d) κ_{tot}, e) κ_{lat}, and f) zT with multilayer structure.

confirms the hypothesis that a thicker multilayer might suppress the κ_{lat} more effectively, decreasing to 9.5 W m^{-1}·K at 673 in the Z44/A11/Z44 sample. The temperature-dependent zT of the optimum multilayer coated samples is demonstrated in Figure 6f. The zT value of the Z44/A11/Z44 sample increased by 128% compared to pure CuNi bulks. Upon comparing our obtained results with those documented in the literature for CuNi alloy systems, it is apparent that the achieved zT at 673 K ranks as the second-highest value reported for this alloy system. However, it is important to consider that CuNi alloys with finer grains and a more optimized composition (such as $Cu_{55}Ni_{45}$) and doping (with Se) have the potential to yield even higher initial zT values. Therefore, it is reasonable to anticipate that by employing the same pristine material conditions reported in studies like Yuan et al.'s, or others,[38–44] further enhancements in zT values are potentially achievable.

As previously discussed, the Al_2O_3 layers can be crystallized during the high-temperature sintering process. According to the literature,[36,37] Al atoms can diffuse into the ZnO structure as a dopant and this might affect the multilayer structure after the sintering process. **Figure 7** demonstrates the EDX-elemental mapping of the Z44/A11/Z44 bulk sample, confirming the homogeneous distribution of Zn and O in the particle's boundaries, demonstrating the excellent conformality of films grown using the ALD technique on the surface of particles. The slight contrast of Al can also be observed revealing that the 11 ALD cycles of Al_2O_3 cause an even distribution of the phase on the surface of CuNi particles (Figure S8, Supporting Information). To precisely analyze the content and distribution of multilayer constituent atoms, the mentioned sample was further studied using scanning transmission electron microscopy (STEM)-EDX and atom probe tomography (APT).

STEM-high angle annular dark field (HAADF) image shows dark contrast in the particle boundaries (**Figure 8**), as the oxide layers have lower atomic numbers. The Al-doped ZnO phase and an Al-poor oxide region are also clearly visualized in Figure 8 showing the different contrast and morphologies. Based on calculations, the thickness of the as-deposited Z44/A11/Z44 sample is estimated to be ≈18.5 nm for ZnO and 1.5 nm for Al_2O_3. As shown in Figure 8a, the oxide layers between CuNi grains are indeed ≈20nm thick. Their compositions are indeed separated from STEM-EDX spectrum imaging (Figure 8b), with one phase enriched in Al (marked by the white arrow, Al/Zn ratio: 0.29), and the other poor in Al (marked by the yellow arrows, Al/Zn ratio: 0.01). The Al-doped ZnO phase is thinner and surrounds the CuNi matrix continuously, whereas the Al-poor oxide region is more rounded and located between the matrix and the Al-doped oxide. The coverage of the Al-doped oxide phase confirms the successful deposition of Al_2O_3 ALD layers within the ZnO layers. The diffusion of Al atoms in most regions of Al-doped ZnO results in the doping effect and causes higher electrical conductivity of the multilayer. It should be noted that the coexistence of the Al-doped ZnO region and Al-poor oxide region is due to the few-cycle numbers of Al_2O_3. As shown in Figure 8c, the island growth of Al_2O_3 occurred and Al_2O_3 layers just deposited on most of the surface area, resulting in the discontinuous distribution of Al_2O_3 between the ZnO layers.

Furthermore, we studied the diffusion of Zn and Al into the CuNi matrix by APT. As shown in Figure S9a,b (Supporting Information), Zn can diffuse deeper into the CuNi matrix (≈2% in the matrix), whereas Al remains very little across the interface of the CuNi matrix (Figure 8d). Nevertheless, the atomic scale microstructural analyses confirm that using ALD accurate regulation of intrinsic characteristics of the modifying

© 2024 The Authors. Advanced Functional Materials published by Wiley-VCH GmbH

layer is possible, resulting in a considerable TE performance enhancement of CuNi thermoelectric material. The present work provides insight into the structural design and synthesis of broadly functional hybrid TE material systems.

3. Conclusion

In summary, ALD-based interface modification has been employed to improve the performance of CuNi alloys by decoupling and optimizing TE parameters. First, the influence of a single kind of oxide coating (ZnO and Al_2O_3) has been thoroughly investigated. The EDX mapping results confirmed the uniform coating on the CuNi powders by ZnO and Al_2O_3 layers. Additionally, a model is proposed to obtain the relationship between the content of Zn/Al and oxide cycle numbers, and experimental results from ICP-OES fit well with the simulation data. This model can be used to estimate the actual composition of coating layers and easily be adapted to other powder ALD processes. For the as-prepared ZnO-coated sample, because of the energy filtering effect, considerable enhancement of S compensates for the electrical loss, resulting in improved PF values in all ZnO-coated samples. Combined with slight suppression on κ_{lat}, the 56% enhancement of zT has been realized in the Z50 sample. For the as-prepared Al_2O_3-coated sample, the Al_2O_3 is detrimental to electrical conduction on the boundaries and the PF of the A10 sample. The significant suppression of κ_{lat} only obtained in low cycle numbers and thicker Al_2O_3 layers provide the thermal conduction path due to the amorphous-to-crystalline transition of Al_2O_3. In order to reduce the electrical resistance of coating layers, the Al_2O_3 layers were inserted into ZnO layers to construct a "multilayer" structure. The EDX results confirmed the existence of ZnO layers. The element scanning proved that the Al atoms diffused into ZnO layers and the Al-doping effect may benefit the increasing of electrical conduction in phase boundaries. In this approach, the higher cycle numbers of ZnO are used to suppress κ_{lat} and maintain the PF. As a result, the zT value of the Z44/A11/Z44 sample increased by 128% compared with pure CuNi bulks, which is nearly the highest zT value among other CuNi works.

This study underscores the potential of ALD-based interface modification as a versatile pathway for decoupling the tightly interrelated parameters and finely tuning the properties of phase boundaries. This approach holds promise not only for CuNi alloys but also for exploring broader applications across various thermoelectric materials. Nevertheless, given the direct influence of numerous processing conditions—including chemical composition, particle size distribution of pristine TE materials, and sintering conditions—on the ultimate TE performance, systematic analyses of these parameters appear indispensable. Such investigations are poised to provide deeper insights into the impact of ALD-based interface modification on the overall performance of CuNi alloy systems, paving the way for future advancements in thermoelectric device design and fabrication.

4. Experimental Section

pALD Process of Coating the CuNi Powders: CuNi powders with <20 µm diameter were purchased from Nanoval GmbH & Co. KG. CuNi were coated in a commercial ALD reactor with a powder rotation option (Veeco Savannah S200) under a base pressure of 0.2 torrs. For each experiment, 5 grams of CuNi powder was transferred into the coating tube in the glove box. The coating details were included in previous publications of the groups.[29,30] To ensure coating uniformity on particles, three strategies were implemented: i) The uniformity of CuNi powder particle size distribution was assessed using particle size analyzer techniques. Additionally, SEM analysis confirmed their spherical shapes, facilitating smooth rolling of the powders over one another, ii) Extended exposure time provided sufficient duration for ALD reactions on the particle surfaces to reach completion, iii) A quartz tumbler served as a rotating apparatus, with an optimal

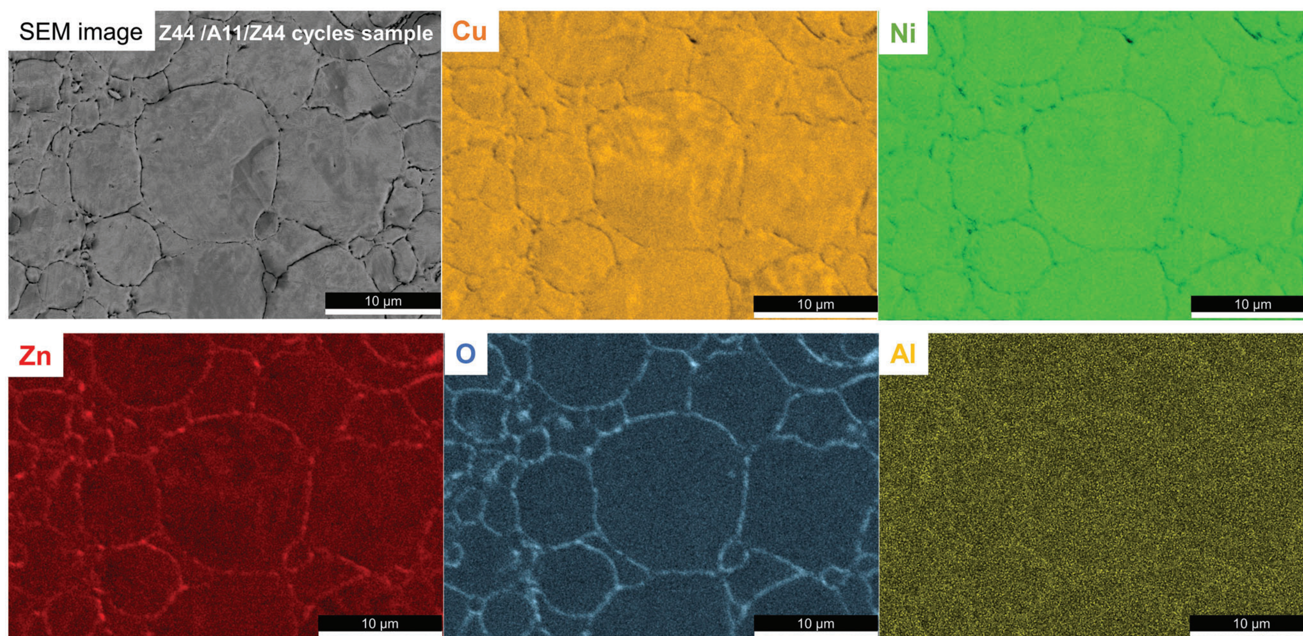

Figure 7. The EDX elemental mapping of the Z44/ A11/ Z44 sample.

© 2024 The Authors. Advanced Functional Materials published by Wiley-VCH GmbH

16163028, 2024, 30, Downloaded from https://onlinelibrary.wiley.com/doi/10.1002/adfm.202314457, Wiley Online Library on [26/09/2024]. See the Terms and Conditions (https://onlinelibrary.wiley.com/terms-and-conditions) on Wiley Online Library for rules of use; OA articles are governed by the applicable Creative Commons License

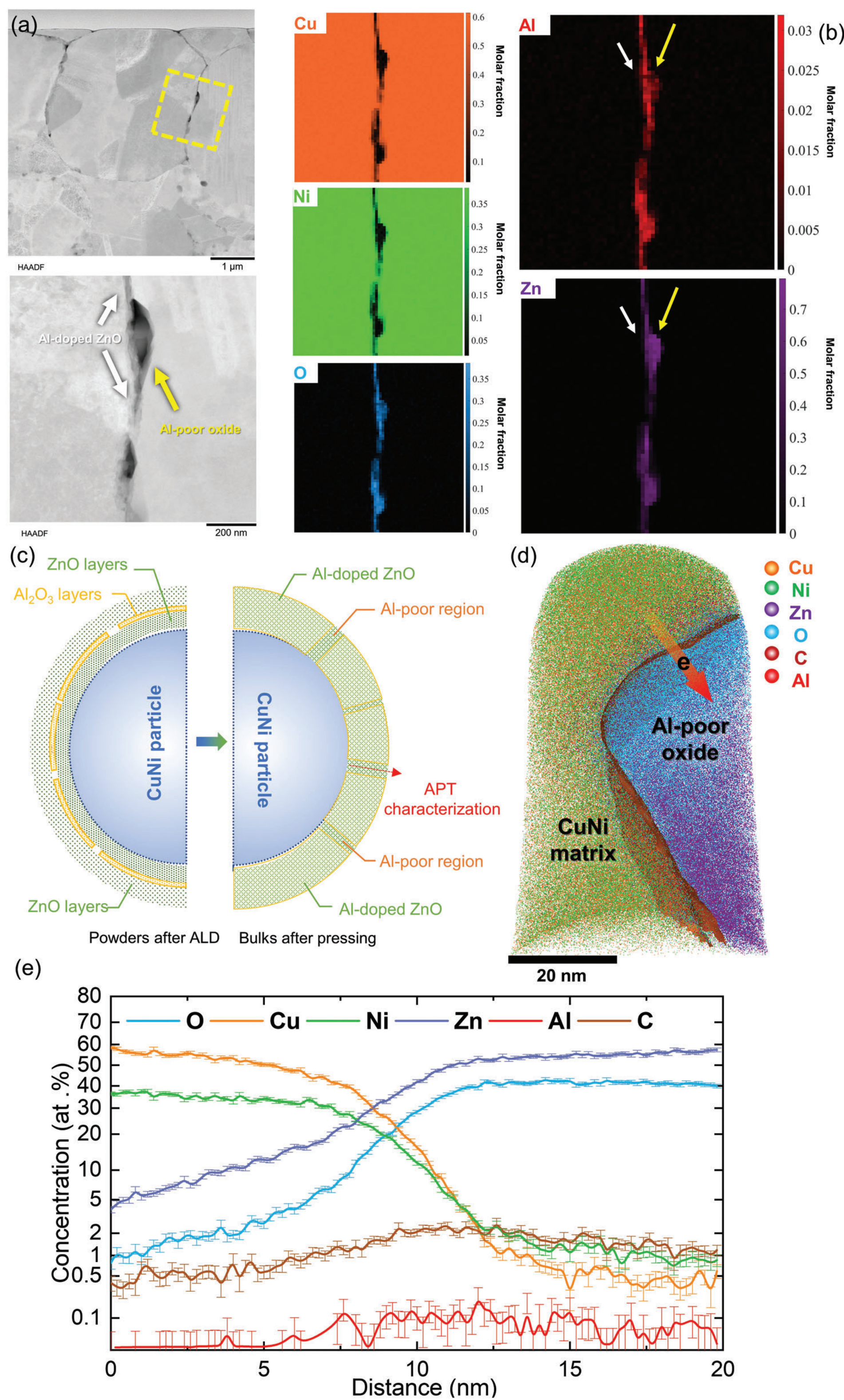

Figure 8. a) HAADF-STEM image of Z44/A11/Z44 specimen and HAADF-STEM image focused on the boundary with b) EDX elemental maps. c) The schematic illustrations for the diffusion of Al. d) 3D atom map of Z44/A11/Z44 sample. e) 1D concentration profile along d direction in (d).

 © 2024 The Authors. Advanced Functional Materials published by Wiley-VCH GmbH

16163028, 2024, 30, Downloaded from https://onlinelibrary.wiley.com/doi/10.1002/adfm.202314457, Wiley Online Library on [26/09/2024]. See the Terms and Conditions (https://onlinelibrary.wiley.com/terms-and-conditions) on Wiley Online Library for rules of use; OA articles are governed by the applicable Creative Commons License

rotation speed of 2 rpm, allowing gases to access all sides of the particle surfaces. Al_2O_3 and ZnO layers were deposited using trimethylaluminum (TMA, 97%, Aldrich), diethylzinc (DEZ, Zn ≥ 52.0%, Aldrich), as ALD precursors at 423 K, reacting with H_2O as an oxidant. All of the precursors were kept at room temperature. The pulse/purge times were as follows: 0.015/15 s for TMA, DEZ, and H_2O. The precursor was supplied to the chamber with a 40 sccm flow of N_2 gas.

Phase Identification and Microstructure Characterization: The size of CuNi particles was checked with a particle size analyzer (Camsizer X2). The inductively coupled plasma-optical emission spectrometry (ICP-OES) measurements were conducted with an iCAP 6500 Duo View (Thermo Fisher Scientific) after aqueous acidic digestion. XRD measurements for bulk samples and thin films were performed using Bruker D8 (Co X-ray source) to examine the samples' phase purity and crystal structure. The densities and thickness of films are calculated based on the results of X-ray reflectivity (XRR) measured by Philips X'Pert pro MRD. The thickness of thin films is determined again by field emission scanning electron microscopy (SEM, Sigma300-ZEISS). A dual-beam focused ion beam (FIB)—scanning electron microscopy (SEM) system (Thermo Fisher Scientific Scios2) was used to fabricate the specimens for STEM and APT. HAADF-STEM imaging was conducted using a Titan Themis microscope (Thermo Fisher Scientific) at 300 kV operation voltage. STEM-EDX spectrum imaging is acquired using a SuperX detector, and multivariate statistical analysis[48] was applied to reduce the noise and separate areas with different compositions. APT analysis was performed using a local electrode atom probe (CAMECA LEAP 5000 XS) in a pulsed laser mode at a specimen base temperature of 60 K. The laser pulse energy, detection rate, and frequency were set to 50 pJ, 1%, and 125 kHz, respectively. Data reconstruction and analyses were done with the AP Suite 6.3, provided by CAMECA Instruments.

Thermoelectric Measurement: The powders with different coated layers were pressed into pellets by spark pressing sintering (AGUS-PECS SPS-210Gx) at 1073 K for 10 min in a vacuum with a uniaxial pressure of 50 MPa. After polishing both sides, the obtained pellets were directly used to measure thermoelectric properties. The standard four-probe method measured the temperature-dependent S and ρ (LSR-3, Linseis). The laser flash method measured the temperature-dependent thermal diffusivity (λ) under a helium atmosphere (LFA 1000, Linseis). The density (D) of the samples was measured by the Archimedes method, and the heat capacity (C_p) was calculated using the Dulong–Petit law. The thermal conductivity (κ_{tot}) was calculated according to the relation $\kappa_{tot} = \lambda \cdot D \cdot C_p$.

Supporting Information

Supporting Information is available from the Wiley Online Library or from the author.

Acknowledgements

This work was supported by the Program of Collaborative Research Centers in Germany (Grant No. SFB 1415), the European Union's Horizon 2020 Research and Innovation Program under grant agreement No 958174 and Deutsche Forschungsgemeinschaft DFG (Project No 516355940).

Conflict of Interest

The authors declare no conflict of interest.

Author Contributions

S.H. designed the research; S.H. and A.B. prepared the pALD samples; C.J. and S.Z. performed the STEM and APT characterizations; S.H. measured the thermoelectrical properties measurement; S.H. conducted the measurement of thin film properties and X.Z. analyzed the data; S.H., R.H., Z. R., and K.N. prepared the manuscript and everyone commented on the manuscript.

Data Availability Statement

The data that support the findings of this study are available on request from the corresponding author. The data are not publicly available due to privacy or ethical restrictions.

Keywords

atomic layer deposition, energy filtering, grain boundary engineering, phonon scattering, thermoelectric materials

Received: November 16, 2023
Revised: February 26, 2024
Published online: April 4, 2024

[1] H.-Y. Pu, R.-Q. Xie, Y. Peng, Y. Yang, S.-Y. He, J. Luo, Y. Sun, S.-R. Xie, J. Luo, *Adv. Manuf.* **2019**, *7*, 278.
[2] S. He, Y. Yang, Z. Li, J. Zhang, C. Wang, W. Zhang, J. Luo, *Sci. China Mater.* **2021**, *64*, 1751.
[3] S. He, Y. Li, L. Liu, Y. Jiang, J. Feng, W. Zhu, J. Zhang, Z. Dong, Y. Deng, J. Luo, W. Zhang, G. Chen, *Sci. Adv.* **2020**, *6*, eaaz8423.
[4] X. Qi, J. Chen, K. Guo, S. He, J. Yang, Z. Li, J. Xing, J. Hu, H. Luo, W. Zhang, J. Luo, *Chem. Eng. J.* **2019**, *374*, 494.
[5] S. He, A. Bahrami, P. Ying, L. Giebeler, X. Zhang, K. Nielsch, R. He, *J. Mater. Chem. A* **2022**, *10*, 13476.
[6] T. Zhu, Y. Liu, C. Fu, J. P. Heremans, J. G. Snyder, X. Zhao, *Adv. Mater.* **2017**, *29*, 1605884.
[7] C. Hu, K. Xia, C. Fu, X. Zhao, T. Zhu, *Energy Environ. Sci.* **2022**, *15*, 1406.
[8] L. You, Z. Li, Q. Ma, S. He, Q. Zhang, F. Wang, G. Wu, Q. Li, P. Luo, J. Zhang, J. Luo, *Research* **2020**, *2020*, 1736798.
[9] L. Jun, H. Shi-Yang, L. Zhi-Li, L. Yong-Bo, W. Feng, Z. Ji-Ye, *J. Inorg. Mater.* **2019**, *34*, 247.
[10] T. Luo, F. Serrano-Sánchez, H. Bishara, S. Zhang, R. Bueno Villoro, J. J. Kuo, C. Felser, C. Scheu, G. J. Snyder, J. P. Best, G. Dehm, Y. Yu, D. Raabe, C. Fu, B. Gault, *Acta Mater.* **2021**, *217*, 117147.
[11] S. Li, Z. Huang, R. Wang, W. Zhao, J. Luo, Y. Xiao, F. Pan, *ACS Appl. Mater. Interfaces* **2021**, *13*, 51018.
[12] S. Li, J. Jiang, Z. Ma, Y. Chen, L. Li, J. Wang, C. Wang, *ACS Appl. Energy Mater.* **2021**, *4*, 9751.
[13] S. He, S. Lehmann, A. Bahrami, K. Nielsch, *Adv. Energy Mater.* **2021**, *11*, 2101877.
[14] W. Y. Chen, X. L. Shi, J. Zou, Z. G. Chen, *Small Methods* **2022**, *6*, 2101235.
[15] Z. Chen, X. Zhang, Y. Pei, *Adv. Mater.* **2018**, *30*, 1.
[16] A. W. Weimer, *J. Nanoparticle Res.* **2019**, *21*, 9.
[17] C. Marichy, M. Bechelany, N. Pinna, *Adv. Mater.* **2012**, *24*, 1017.
[18] X. Y. Zhao, X. Shi, L. D. Chen, W. Q. Zhang, S. Q. Bai, Y. Z. Pei, X. Y. Li, T. Goto, *Appl. Phys. Lett.* **2006**, *89*, 092121.
[19] M. Ito, T. Tanaka, S. Hara, *J. Appl. Phys.* **2004**, *95*, 6209.
[20] M. Xie, X. Sun, C. Zhou, A. S. Cavanagh, H. Sun, T. Hu, G. Wang, J. Lian, S. M. George, *J. Electrochem. Soc.* **2015**, *162*, A974.
[21] Z. Xiong, X. Chen, X. Zhao, S. Bai, X. Huang, L. Chen, *Solid State Sci.* **2009**, *11*, 1612.
[22] X. Wang, *Chem. Mater.* **2021**, *33*, 6251.
[23] D. J. Hagen, M. E. Pemble, M. Karppinen, *Appl. Phys. Rev.* **2019**, *6*, 041309.
[24] Y. Kim, W. J. Woo, D. Kim, S. Lee, S. Chung, J. Park, H. Kim, *Adv. Mater.* **2021**, *33*, 2005907.
[25] C. Shen, Z. Yin, F. Collins, N. Pinna, *Adv. Sci.* **2022**, *9*, 2104599.
[26] V. Miikkulainen, M. Leskelä, M. Ritala, R. L. Puurunen, *J. Appl. Phys.* **2013**, *113*, 021301.

© 2024 The Authors. Advanced Functional Materials published by Wiley-VCH GmbH

16163028, 2024, 30, Downloaded from https://onlinelibrary.wiley.com/doi/10.1002/adfm.202314457, Wiley Online Library on [26/09/2024]. See the Terms and Conditions (https://onlinelibrary.wiley.com/terms-and-conditions) on Wiley Online Library for rules of use; OA articles are governed by the applicable Creative Commons License

[27] Y. Hu, J. Lu, H. Feng, *RSC Adv.* **2021**, *11*, 11918.
[28] I.-K. Oh, T. E. Sandoval, T.-L. Liu, N. E. Richey, S. F. Bent, *Chem. Mater.* **2021**, *33*, 3926.
[29] S. He, J. Yang, A. Bahrami, X. Zhang, R. He, M. Hantusch, S. Lehmann, K. Nielsch, *ACS Appl. Energy Mater.* **2022**, *5*, 4041.
[30] S. He, A. Bahrami, X. Zhang, I. G. Martínez, S. Lehmann, K. Nielsch, *Adv. Mater. Technol.* **2022**, *7*, 2100953.
[31] S.-S. Lim, K.-C. Kim, S. Lee, H.-H. Park, S.-H. Baek, J.-S. Kim, S. K. Kim, *Coatings* **2020**, *10*, 572.
[32] S. Li, Y. Liu, F. Liu, D. He, J. He, J. Luo, Y. Xiao, F. Pan, *Nano Energy* **2018**, *49*, 257.
[33] S. Kim, J. An, W.-J. Lee, S. Kwon, W. Nam, N. Du, J.-M. Oh, S.-M. Koo, J. Cho, W. Shin, *Nanomaterials* **2020**, *10*, 2270.
[34] Y. Zhang, S. Li, F. Liu, C. Zhang, L. Hu, W. Ao, Y. Li, J. Li, H. Xie, Y. Xiao, F. Pan, *J. Mater. Chem. A* **2019**, *7*, 26053.
[35] S. Li, Z. Huang, R. Wang, C. Wang, W. Zhao, N. Yang, F. Liu, J. Luo, Y. Xiao, F. Pan, *J. Mater. Chem. A* **2021**, *9*, 11442.
[36] J. Felizco, M. Uenuma, T. Juntunen, J. Etula, C. Tossi, Y. Ishikawa, I. Tittonen, Y. Uraoka, *ACS Appl. Mater. Interfaces* **2020**, *12*, 49210.
[37] P. Banerjee, W.-J. Lee, K.-R. Bae, S. B. Lee, G. W. Rubloff, *J. Appl. Phys.* **2010**, *108*, 043504.
[38] K. Guo, J. Zhang, Y. Zhang, L. Liu, S. Yuan, Y. Jiang, J. Luo, J.-T. Zhao, *ACS Appl. Energy Mater.* **2021**, *4*, 5015.
[39] M. Wolf, J. Flormann, T. Steinhoff, G. Gerstein, F. Nürnberger, H. J. Maier, A. Feldhoff, *Alloys* **2022**, *1*, 3.
[40] H. Kang, Z. Yang, X. Yang, J. Li, W. He, Z. Chen, E. Guo, L.-D. Zhao, T. Wang, *Mater. Today Phys.* **2021**, *17*, 100332.
[41] J. Mao, Y. Wang, H. S. Kim, Z. Liu, U. Saparamadu, F. Tian, K. Dahal, J. Sun, S. Chen, W. Liu, Z. Ren, *Nano Energy* **2015**, *17*, 279.
[42] I. Paulraj, V. Lourdhusamy, C.-J. Liu, *Chem. Eng. J.* **2022**, *446*, 137083.
[43] C. Jia, X. Xu, L. Zhong, D. Kang, P. Shen, B. Xu, J. Bai, F. Xue, K. Yin, B. Zhu, L. Tao, *ACS Appl. Energy Mater.* **2022**, *5*, 5044.
[44] M. Yuan, L. Sun, X. W. Lu, P. Jiang, X. H. Bao, *Mater. Today Phys.* **2021**, *16*, 100311.
[45] J. W. Park, S. J. Kim, *J Korean Phys Soc* **2005**, *47*, https://doi.org/10.3938/jkps.47.182.
[46] C. Barbos, D. Blanc-Pelissier, A. Fave, E. Blanquet, A. Crisci, E. Fourmond, D. Albertini, A. Sabac, K. Ayadi, P. Girard, M. Lemiti, *Energy Procedia* **2015**, *77*, 558.
[47] S. Jakschik, U. Schroeder, T. Hecht, M. Gutsche, H. Seidl, J. W. Bartha, *Thin Solid Films* **2003**, *425*, 216.
[48] S. Zhang, C. Scheu, *Microscopy* **2018**, *67*, i133.

© 2024 The Authors. Advanced Functional Materials published by Wiley-VCH GmbH

16163028, 2024, 30, Downloaded from https://onlinelibrary.wiley.com/doi/10.1002/adfm.202314457, Wiley Online Library on [26/09/2024]. See the Terms and Conditions (https://onlinelibrary.wiley.com/terms-and-conditions) on Wiley Online Library for rules of use; OA articles are governed by the applicable Creative Commons License